



Research article

Photocatalytic degradation of acid blue 74 by Co: WO₃ nanoparticles: Kinetics and response surface methodology studies

Leila Montazerghaem^a, Mitra Keramatifarhodbonab^{b,*}, Alireza Naeimi^c^a Faculty of Chemical, Petroleum and Gas Engineering, Semnan University, Semnan, Iran^b Department of Nanomaterials and Nanotechnology, Institute for Color Science and Technology, Iran^c Department of Polymer Engineering, Nanostructured Materials Research Center, Sahand University of Technology, Tabriz, Iran

ARTICLE INFO

Keywords:

Wastewater treatment
WO₃: Co photocatalyst
Solution combustion method
Acid blue 74 degradation
RSM modeling

ABSTRACT

Energy-efficient sol-gel synthesis was achieved through the microwave assisted self-combustion route to produce hexagonal Tungsten oxide semiconductor (WO₃). The photocatalytic activity was enhanced by doping Cobalt (Co) into the crystalline structure of the nanoparticle, which were subsequently sintered at 400 °C for an hour. The structural and morphological properties of the Co-doped WO₃ were revealed using X-ray diffraction (XRD) characterization. The nanoparticles exhibited an amorphous structure before annealing, due to the short heating time during combustion synthesis. Sintering the nanoparticle transformed the nanoparticle from a monoclinic phase to orthorhombic phase structure. Additional analysis techniques, including scanning electron microscopy (SEM), transmission electron microscopy (TEM) and energy dispersive X-ray spectrum analysis (EDS).

To assess the photocatalytic performance of these particles, Acid Blue 74 (AB 74) was employed in photodegradation experiments under UV light irradiation within a semi-continuous reactor.

The photodegradation of dye molecules was evaluated utilizing a UV-Vis spectrophotometer, and the mineralization efficiency of the dye was determined through total organic carbon analysis (TOC). The results indicated that the dimension of the synthesized nano catalyst fell within the range of 70–120 nm, and it exhibited the ability to completely degrade a solution with an initial dye concentration of 20 ppm within 60 min. Various parameters affecting the photocatalytic reaction, including the photocatalyst dosage, initial dye concentration, pH and temperature of the dye solution were also investigated. The experiments were designed using Response surface methodology (RSM), through which a mathematical model for the dye removal process was developed.

1. Introduction

The wastewater treatment process, which contains organic solvents and sludge production as a by-product of sewage treatment, has become a significant challenge for the safety of the aquatic ecosystem due to its high toxicity and severe effects on human health. Conventional sewage treatment methods, including flocculation, adsorption, membrane separation, solvent extraction, and biodegradation are commonly used [1,2].

* Corresponding author.

E-mail address: keramatif.mitra@gmail.com (M. Keramatifarhodbonab).

<https://doi.org/10.1016/j.heliyon.2024.e24789>

Received 2 September 2023; Received in revised form 13 January 2024; Accepted 15 January 2024

Available online 21 January 2024

2405-8440/© 2024 The Authors. Published by Elsevier Ltd. This is an open access article under the CC BY-NC-ND license (<http://creativecommons.org/licenses/by-nc-nd/4.0/>).

Wang et al. reported the usage of Polyurethane (PU) sponge with bamboo charcoal powder with superhydrophobic/oleophilic surface as an adsorbent for oil-water separation [3]. Pang et al. have reported persulfate oxidation process through the activation of peroxymonosulfate (PMS) using natural wood derived carbon embedded with Fe/Co bimetallic sites for degrading ciprofloxacin (CIP) pollutant degradation [4]. A significant challenge of using PMS is its ability to degrade only certain electron-rich moieties of pollutants, and the rate of contaminant removal is extremely low if the activation step is incomplete [1]. However, these processes have serious disadvantages such as low adsorption efficiency, lack of selectivity, and non-reusability. Therefore, the invention of new types of degradation methods without these restrictions, such as photocatalytic degradation has been widely investigated [2].

Traditional methods of water treatment, including adsorption and precipitation, are not appropriate strategies for removing toxic substances and volatile organic compounds (VOCs) from water [3,4]. Advanced oxidation processes (AOPs), such as Fenton oxidation [5], electrochemical oxidation, photocatalysis have been studied for their ability to generate reactive, and non-selective radicals compared to adsorption, which is expected to have selectivity and large adsorption capacity [2,3]. Among these methods, photocatalysis, utilizing clean and inexhaustible light, has emerged as a promising AOP technique through oxidant precursor activation. It can effectively eliminate micropollutants via generating highly reactive radical species, such as sulfate ($\text{SO}_4^{\bullet-}$), hydroxyl ($\bullet\text{OH}$) and superoxide ($\text{O}_2^{\bullet-}$) radicals [6]. Semiconductor-based heterogeneous photocatalysis falls within the category of AOPs, targeting the elimination of the pollutants from wastewater, with a specific focus on discharging organic dye pollutants.

Organic dyes are considered as one of the largest categories of water pollutants [7]. In recent decades, the production and usage of synthetic dyes have increased in various industries such as textiles, paper, photography, pharmaceutical, food, and cosmetics. Due to their rigid chemical structure, they are challenging for biodegradation, and conventional water treatment processes are unable to eliminate these elements from the environment. They possess stable structures that persist in harsh conditions such as high temperature, and light [8].

Approximately 1–15% of the organic dye compounds used in these industries become waste and end up in wastewater, returning to the environment [9,10]. The presence of even small amount of the dye in wastewater is highly dangerous. In addition, the organic compounds present in these dyes pose a serious risk to the environment due to their toxic and carcinogenic structure [11–13]. For instance, Methylene Blue (MB) is one of the most common dyes used in industry for various purposes, such as coloring silk, wool, cotton, and paper. It is highly water-soluble, non-biodegradable, and very stable in water solutions at room temperature. Additionally, it is toxic to the human being above a certain concentration [14].

In this regard, the wastewater treatment process is crucial for the pollution control, involving two main steps: (1) separation, and (2) partial or complete mineralization of dyes, along with the destruction of their chemical structure [15]. In the first step, physical processes such as sedimentation, floatation and filtration or membrane filtration (NF, UF, RO)), as well as physiochemical treatment processes such as adsorption, and chemical precipitation, are employed to separate contaminants. However, it is important to note that these methods only transfer pollutants to another phase [16]. A further degradation step of pollutants via biological or chemical methods is required to complete the purification of wastewater. Major organic dyes are not biodegradable; Therefore, among the various wastewater treatment methods such as Advanced Oxidation Processes (AOPs) have [11,15].

In recent years, the photodegradation of water pollutants has focused on using more stable, and efficient photocatalysts. This involves producing heterojunction species to hinder the charge recombination and increase the optical absorption of the photocatalysts. The application of carbon-based materials, including carbon nanotubes (CNTs), graphene, and carbon fibers as a metal-free and visible-light bases for the photocatalysts, has been reported due to their high specific surface area and efficient charge transfer ability. However, they all suffer from inadequate utilization of visible light energy usage resulting from a wide bandgap [17].

Semiconductors can serve as photocatalysts due to their appropriate electronic structure, light absorption properties, electric charge transfer ability and excited state lifetime. One of the semiconductors that has recently attracted attention is WO_3 [18,19].

Recent studies have shown that the assembly of two semiconductors appears to be an effective way of harnessing the potential of both semiconductors as a Z-scheme photocatalytic system. In this system, charge transfer follows a different pathway, suppressing weak oxidative holes and reductive electrons [20].

Aziz et al., have investigated the WO_3/ZnO composite with an orthorhombic phase of WO_3 , which has a lower band-gap energy compared to ZnO . This composite can degrade 94 % and 85.7 % of Methylene Blue and Rhodamine Blue, respectively [19]. In another study on the photocatalytic degradation of a group of dyes, including basic violet 10 (BV10), acid blue 9 (AB9), acid orange 7 (AO7), and acid red 1 (AR1), photocatalysis was conducted using W-doped titania as the photocatalytic semiconductor. The optimum result for the photocatalytic degradation was BV10 (49.77 %), AB9 (14.95 %), AB9 (14.95 %), AO7 (2.12 %), and AR1 (0.54 %) [21]. The method used for semiconductor synthesis has a significant impact on the particle size, morphology, and surface area of produced particles. Various methods have been employed for the synthesis of WO_3 , including precipitation method [22], sol-gel [23], thermal decomposition [24], and ion-exchange methods [25–27]. Microwave-assisted solution combustion is a new technique known for its ability to produce nanoparticles by providing conventional heating, uniform elevated temperature, and a rapid process of the WO_3 synthesis [28]. This method is an advantageous option for the reactions that are sensitive to temperature [29,30]. Microwave-assisted synthesis is proven to be a stable and selective technique, particularly in the preparation of Co doped WO_3 nanoparticles. It is a quick and efficient process, saving time and energy. Microwave-assisted synthesis is a suitable method for producing nanoparticles due to its high heating rate, short processing duration, low energy, and time consumption by generating uniform heating within the material. Notably, the synthesis of WO_3 nanoparticles was performed using the microwave-assisted combustion method with citric acid as the combustion fuel [29].

Doping a semiconductor with metal elements can postpone the electron–hole pairs' recombination time, and thus improving the photocatalytic activity of the semiconductor. In this study, AB 74 was used as the synthetic dye to investigate the photocatalytic efficiency of the synthesized photocatalyst. AB 74 dye is a water-soluble blue dye and an indigo derivative. This dye has wide

applications in the textile industry due to its ability to dye wool fibers and cotton clothes (blue jeans). Indigo carmine is a highly toxic indigoid dye. It causes injury for cornea and conjunctiva when it contacts the eyes and skin [30–32].

2. Material and methods

2.1. Preparation of catalyst

Co doped WO_3 nanoparticles were synthesized using the *microwave-assisted solution combustion* method. Tungsten powder with 99.99 % purity (Sigma-Aldrich), and Cobalt nitrate hexahydrate ($\text{Co}(\text{NO}_3)_2 \cdot 6\text{H}_2\text{O}$) (Sigma-Aldrich) with 98 % purity, were used as the precursors. 3g of Tungsten powder was dissolved in 50 ml of 37 % H_2O_2 . Then, 0.2g of Cobalt nitrate salt was added to the solution and it was stirred until the salt was completely dissolved. 1.5 g of citric acid was added as combustion fuel. To evaporate the water of the solution and form a gel, the obtained solution was placed on a heater stirrer for several minutes. Subsequently, the resulting gel was placed under the microwave irradiation at a power of 900 W to combust and produce the dry foam (Fig. 1). All the materials used in this process were of high purity materials and were purchased from Merck and Sigma-Aldrich.

2.2. Characterization

XRD is a technique to provide chemical data for elemental and phase analysis. XRD is a powerful tool for the phase identification based on their crystal structures, and the crystalline phase of the material including size, shape, crystal orientation, and surface characterization can be calculated from the diffraction pattern [33,34]. Therefore, the characterization of the obtained product was investigated with the XRD analysis. Investigating the crystal structure of the catalyst was performed by X-ray diffraction STOE Stadi P model with $\text{Cu-K}\alpha$ ($\lambda = 1.54056 \text{ \AA}$) radiation in diffraction angle (2θ) range of 10° – 100° with a typical step size of 0.026° .

SEM profoundly determines the particle size, distribution, shape, and overall surface morphology of a catalyst. In this regard, the morphologies of the as-prepared Co doped WO_3 nanoparticles were analyzed by (SEM) (LEO 1455 VP-SEM) [35].

TEM is a tool to characterize the nanoscale of all types of materials chemically and structurally. For this reason, we used (EM 900 TEM, Zeiss, Germany) to investigate the particle size of photocatalyst.

The Zeiss Sigma Family FE-SEM, equipped with an Oxford Instrument EDS detector was used for elemental analysis of the produced photocatalysts.

2.3. Evaluation of photocatalytic activity

The photocatalytic performance of the synthetic particles was evaluated with the photodegradation of AB 74, (Merck) (Table 1).

The photocatalytic tests were performed in a Pyrex tubular reactor with a volume of 325 ml, the input volume flow rate was $49.75 \times 10^{-6} \text{ (m}^3/\text{s)}$, and the fluid flow inside the reactor was laminar with a Reynolds number of 260. The reactor was equipped with an ultraviolet low pressure mercury lamp (253.7 nm, OSRAM) located at the center of this reactor which protected within the quartz tube with an outer diameter of 3 cm. (Fig. 2).

The collected samples from the reactor output effluent were centrifuged at 4500 rpm at specified intervals, and the absorbance of the samples was determined by a UV–visible spectrometer, one beam CECIL and two beam PerkinElmer lambda 25.

To calculate the decolorization and degradation efficiency of the photocatalyst during the reaction, equation (1) has been used, respectively.

$$\text{Decolourization(\%)} = \frac{C_0 - C}{C_0} \times 100 \quad (1)$$

where C_0 and C correspond to the initial and final concentration of dye before and after a certain irradiation time, respectively.

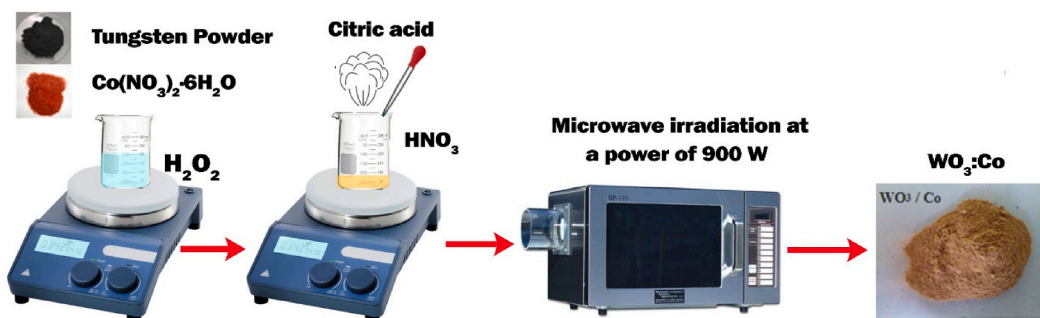
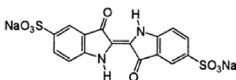


Fig. 1. Synthesis of the nano photocatalyst.

Table 1
AB 74 properties.

Molecular weight	λ_{\max}	Molecular formula	Molecular structure
466.35 g mol ⁻¹	617 nm	C ₁₆ H ₈ N ₂ Na ₂ O ₆ S ₂	

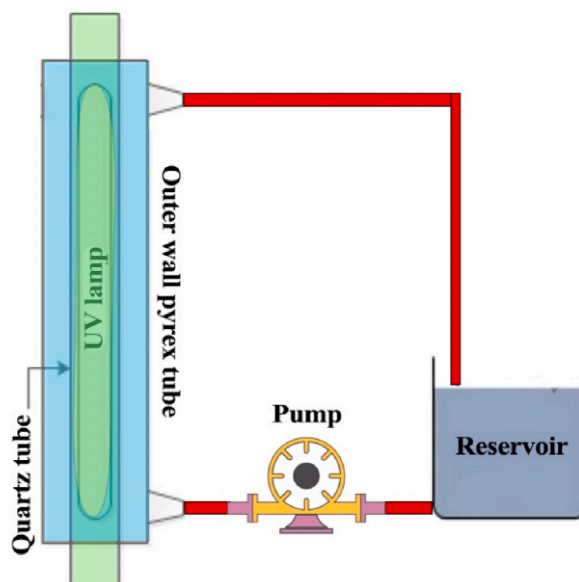


Fig. 2. Photocatalytic reactor's scheme.

2.4. Experimental design method

In this study, Response Surface Methodology (RSM) was used for the design of experiments. The RSM was first developed and used in 1951 by Box and Wilson to determine the optimal operating conditions for chemical processes. Over the years, this model was developed in several stages to be more applicable in various experimental conditions to extend its application areas [35,36]. For this research, the Minitab 16 software was used to find the optimal conditions. The central composite design (CCD) was utilized to calculate the optimal conditions of the photocatalytic reaction for dye degradation as a function of the main factors. The three factors of catalyst dosage, pH and initial concentration of the dye solution are considered as the most effective parameters in the photocatalytic decolorization efficiency. To find optimal reaction conditions, modeling experiments were conducted based on these three parameters.

This model was defined for three variables, each with three levels comprising 6 axial, 8 full factorial, and 6 center tests resulting in a total of 20 tests. The variables studied in this model include X_1 (initial dye concentration), X_2 (dosage of catalyst), and X_3 (pH of dye solution). The reaction variables are coded according to equation (2) as shown in Table 2 [37].

$$x_i = \frac{X_i - X_{i0}}{\Delta X_i} \quad (2)$$

The relationship between variables and photocatalytic efficiency is defined by the CCD quadratic model in the following equation (3) [38].

Table 2
Experimental magnitude of the model variables.

Variables	Coded factors	Ranges and levels		
		-1	0	1
Dye concentration (ppm)	X_1	20	30	40
Catalyst dosage (g.L ⁻¹)	X_2	0.16	0.2	0.24
pH	X_3	5	7	9

$$Y = b_0 + \sum_{i=1}^k b_i x_i + \sum_{i=1}^k b_{ij} x_i x_j + \sum_{i=1}^k b_{ii} x_i^2 + \varepsilon \quad (3)$$

In this equation, Y represents the response of the model, which, in this research, is the photocatalytic decolorization efficiency. The variable k is defined as the number of variables, b_0 is the constant term, b_i is coefficients of parameters, b_{ij} is interaction coefficients of linear parameters, b_{ii} is coefficients of quadratic parameters and ε is the experimental error. In this study, a total of 20 tests were designed by the RSM.

3. Results and discussion

3.1. Structure of catalysts

In Fig. 3, the XRD results reveal the formation of WO_3 phase. The combustion conditions are characterized by the low temperature and high speed and has no long-range order in its crystal structure. The broad and short peaks in its X-ray diffraction is evidence of the amorphous structure of the Tungsten oxide [39]. However, these short peaks are in accordance with standard cards (Reference code: 01-083-0951), which represents the monoclinic crystalline structure of WO_3 . Doping Co in the Tungsten Oxide crystalline structure is confirmed by exhibiting a slight peak shift compared to the planes of pure WO_3 at (0 0 2), (0 2 0), and (2 0 0). The content of Co added during the synthesis was a minimal 0.1 W%, which is an extremely low percentage, and, in this regard, the correlated peaks of the metal dopant cannot be observed. As a result, the amorphous structure and the size of the crystal lattice can hardly be calculated using the Scherrer formula that certainly will not be accurate. By performing the heat treatment at 400 °C for 1 h, the crystalline structure of Tungsten oxide transformed into an orthorhombic phase with long-range order and sharp peaks. In this case, the average crystallite size of WO_3 and $WO_3:Co$ were calculated using Scherrer equation (4):

$$d = \frac{K \cdot \lambda}{\beta \cdot \cos \theta} \quad (4)$$

Where K is the Scherrer constant, d is the crystallite diameter in nm, λ is the wavelength of the X-ray beam used in nm (1.54 nm), θ is the Bragg angle in degrees and β is the full width at half-maximum peak height in rad. Based on the most intense (002) peak, the crystallite size of WO_3 and $WO_3:Co$ were obtained at about 12.9 and 78.7 nm, respectively [39,40]. It has been found that the addition of doped elements such as (Zn, Co, Fe atoms) in the lattice structure can lead to a reduction in peak intensity. In this study, the radius of Co ion (Co^{2+} : 0.072 nm) is larger than W ions (W^{6+} : 0.06 nm) and the substitution causes an expansion in the crystallinity of the monoclinic structure of WO_3 and makes the monoclinic crystal planes growth [28,39–41].

The photocatalytic test comparison for two samples of Co: WO_3 with monoclinic and orthorhombic phase showed the better photocatalytic performance of the sample with the amorphous structure, so it has been used as a photocatalyst in current study. In addition, heterojunction refers to the cooperation of two semiconductors with dissimilar bandgap energy levels. This heterojunction is advantageous in helping the charge carrier faster within the semiconductors and delaying the electron-hole recombination rate, so the photogenerated electrons will have a longer lifetime. In this regard, WO_3 samples with doped Co reveal an improved photocatalytic performance, along with an amorphous structure of the semiconductor compound [42].

Fig. 4 displays scanning electron microscope images of the synthesized sample. The SEM images show agglomerated structure, where particles can be defined as nano-metric mass that are densely attached to one another (Fig. 4a). This agglomeration is resulted from the low intensity of the combustion and incomplete release of gases caused by organic fuel such as carbon dioxide and nitrate gases (Fig. 4b). Furthermore, the process and the type of reaction are in such a way that the germination rate is higher than the growth rate, leading to the production of nanoparticles. These masses exhibit a high surface area, which is a positive characteristic for applications such as bleaching. Utilizing the software and considering the amorphous morphology type of the sample, the particle size

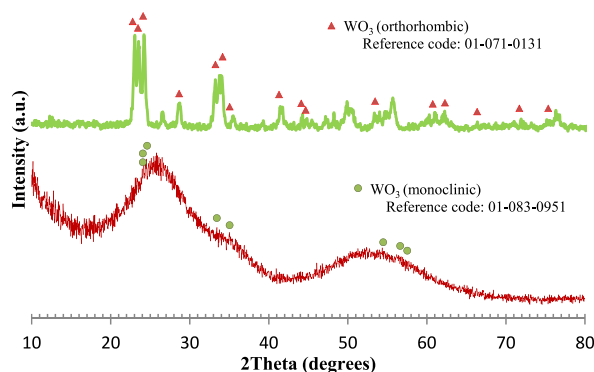


Fig. 3. XRD patterns of $WO_3:Co$ particle.

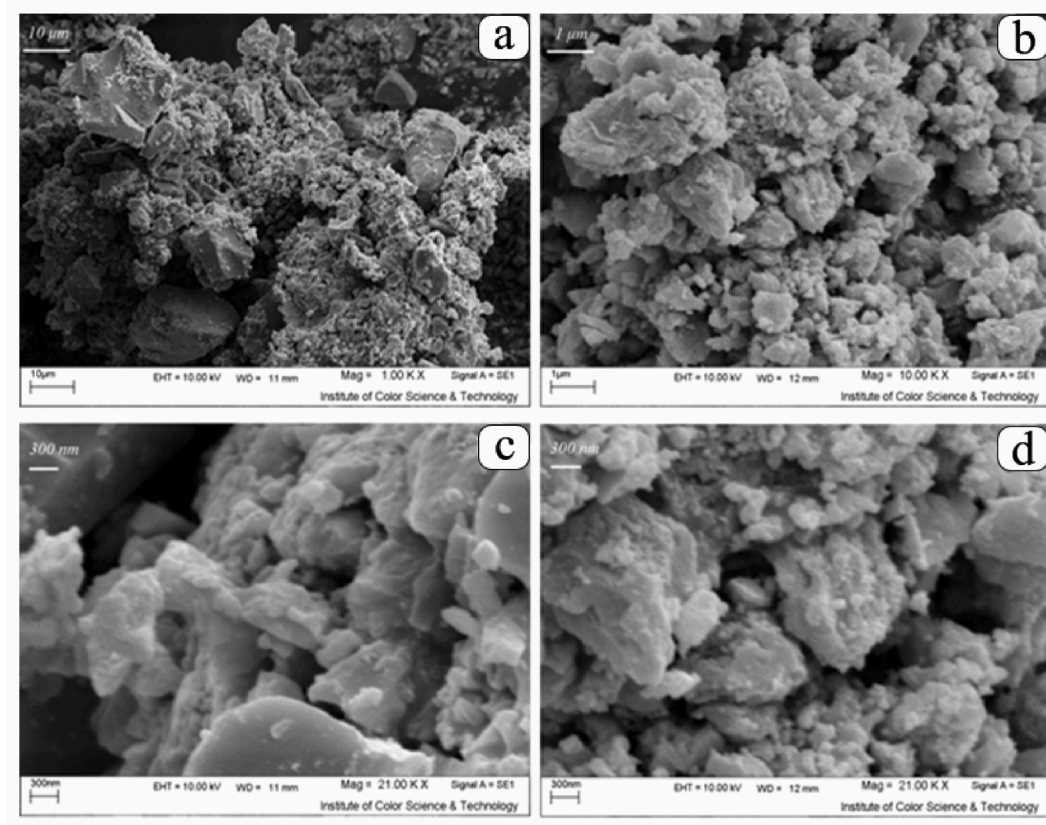


Fig. 4. SEM images of the synthesized sample.

can be estimated within the range of 200–500 nm (Fig. 4c and d).

TEM images of synthesized samples show that the nanoparticles produced by this method are highly agglomerated and have varying particle sizes. Most of the particle sizes are between 70 and 120 nm (Fig. 5a). Fig. 5b indicates that three particles with the size less than 100 nm attached together.

EDS analysis gives information about dopant elements on the photocatalyst surface. The analysis of three different points of the powder's surface reveals the uniform distribution of Co on the catalyst surface. It detects 0.5 wt % of Co on the surface of catalyst (Fig. 6, Table 3).

The absorbance spectrum of the synthesized particles was used to determine the bandgap of the nanoparticles. According to Fig. 7, the light absorption angles of $\text{WO}_3:\text{Co}$ occur at wavelengths of 208 and 260 nm.

In Fig. 8, Tauc plot of the catalyst is presented, where $(\alpha h\nu)^2$ is plotted as a function of $h\nu$, with a bandgap between 4.28 eV. Increasing the bandgap will reduce the amount of absorbed light, but the valence band will be increased to higher energy levels.

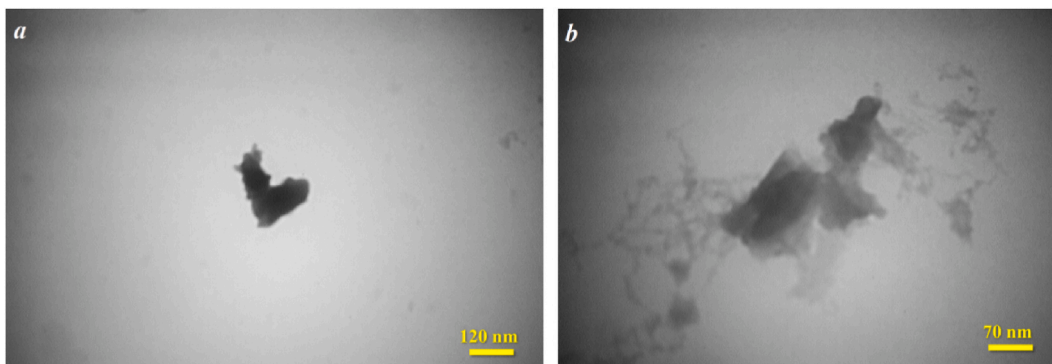


Fig. 5. TEM images of $\text{WO}_3:\text{Co}$.

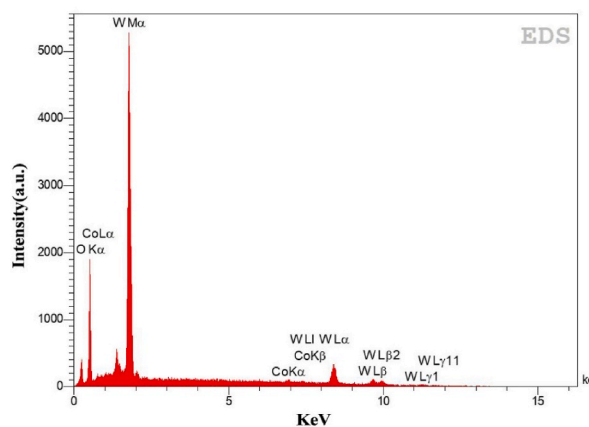


Fig. 6. EDS diagram of catalyst.

Therefore, the oxidation power increases and the electron transfer from WO_3 to the substrate is facilitated. For these reasons, the catalysts with wider bandgap will have a better performance under the UV light [43]. In this equation, h represents Planck's constant, α is the absorbance coefficient, ν is the photon frequency, and n for indirect transitions is equal to 2. The required energy to excite the electrons of the material with this bandgap is supplied by UV light.

3.2. Effect of catalyst dosage

Photodegradation (PD) is a process, in which complex and stable molecular structures deteriorate into smaller, non-poisonous, and lower-weight molecules using solar light across a broad spectrum. The process initiates when photons from the UV, visible or IR spectral ranges are absorbed.

PD is an economical and efficient process that can be used to transform light energy into chemical energy, and then utilize this generated energy for the degradation of organic compounds such as dyes.

Heterogeneous photocatalysis reactions occur on the surface of the semiconductor photocatalyst when exposed to the photons. When these semiconductor photocatalyst are irradiated under light with photon energy higher than their specific band-gap energy, electrons are excited from the valence band (VB) of the nanoparticles (NPs) to the conduction band (CB) and electron-hole pairs are generated (e^-/h^+). To figure out which species react with the dye molecule, the general mechanism of active radical formation and degradation is explained below:



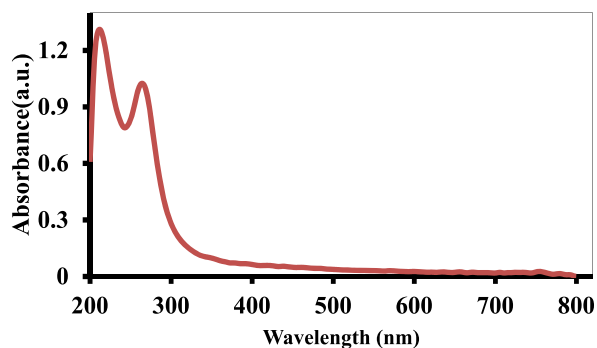
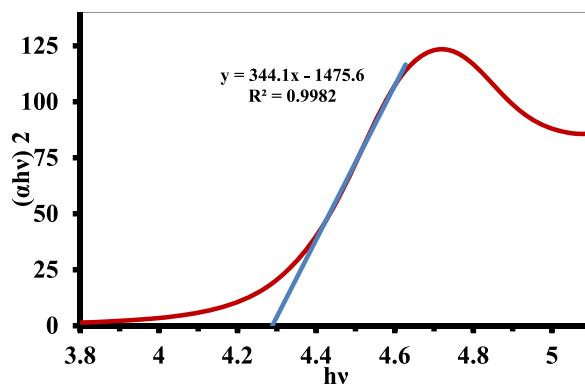
According to the reactions above, the generated holes react with H_2O , and as a result hydroxyl radicals (oxidative potential +2.8 V) are formed. On the other hand, conduction band electrons are trapped by O_2 molecules to create super oxide radicals ($\cdot O_2^-$) [44,45].

To determine the optimal catalyst dosage, we performed the photocatalytic dye degradation tests of the dye solutions with an initial

Table 3

Composition of the elements of the photocatalyst.

Element	Line	Int	wt.%	A%
C	Ka	35.3	8.87	28.86
O	Ka	205	19.47	53.52
Co	Ka	8.1	0.49	0.37
W	La	131.2	72.15	17.26
			100.00	100.00

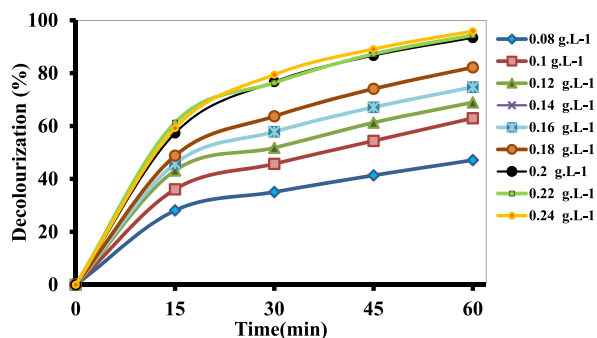
Fig. 7. UV-Vis spectra of WO₃:Co photocatalyst.Fig. 8. Tauc plot of WO₃:Co nanoparticles.

concentration of 20 ppm. The reaction time was conducted for 60 min, using different catalyst dosages ranging from 0.08 g. L⁻¹ to 0.24 g. L⁻¹. The number of the active sites on the WO₃:Co surface increases as the amount of photocatalyst and the catalytic reaction rate increases correspondingly.

Fig. 9 indicates the enhancement of photocatalytic performance of WO₃:Co particles as the catalyst dosage is increased from 0.08 g. L⁻¹ to 0.2 g. L⁻¹. This trend continues until an increase in the dosage of the catalyst causes light scattering, preventing the penetration of light photons onto the photocatalyst surface [46]. If the catalyst dosage exceeds 0.2 g. L⁻¹, the photocatalytic reaction rate remains unchanged. Therefore, the optimal dosage of the catalyst for WO₃:Co particulate is 0.2 g. L⁻¹. An experiment involving the adsorption of the synthesized catalyst in the dark for 30 min showed less than 3% of the dye adsorption, which was negligible.

3.3. Effect of pH

Due to the zeta potential of the catalyst, the pH of the dye solution can contribute to the dye adsorption on the catalyst's surface. A decrease in reactants on the surface of catalysts leads to a decline in the photocatalytic reaction rate. To investigate the effect of pH of AB 74 solution's pH, the photocatalytic efficiency of WO₃:Co was investigated in an acidic environment (pH = 5), a neutral pH of the

Fig. 9. Decolorization of the dye using various (catalyst dosage = 0.08 g. L⁻¹ - 0.24 g. L⁻¹, t = 60 min, [AB 74]₀ = 20 ppm).

dye solution (pH = 7), and an alkaline environment (pH = 9) with a catalyst dosage of 0.2 g. L⁻¹ and an initial dye concentration of 20 ppm in the effluent.

According to Fig. 10, the pH of the AB 74 solution has a slight effect on the photocatalytic efficiency of WO₃: Co nanoparticles. Decolorization efficiency in the dye solution with an acidic pH is slightly higher than other pH levels. (Fig. 10). It is difficult to interpret the impact of pH on the photodegradation of the organic compound in solution, however, the results reveal that due to the nature of AB 74, its dissociation capacity, the charge distribution on the surface of the Co: WO₃ nano photocatalyst, and also the oxidation power of the synthesized Co: WO₃ attributed to their cooperated valence band, it can be better decomposed in acidic environment [47].

3.4. Effect of Initial dye concentration

The effect of the initial dye concentration on the photocatalytic reaction rate was evaluated in the dye solution of IC with a range of initial dye concentration of 10 ppm–60 ppm, using a catalyst dosage of 0.2 g. L⁻¹. As shown in Fig. 11, an increase in the AB 74 concentration reduces the photocatalytic efficiency of WO₃: Co. Initially, an increase in the initial dye concentration enhances the number of reactants on the catalyst's surface, improving the photocatalytic reaction rate. Another explanation for the decrease of degradation rate with higher dye concentrations could be that concentrated pollutant solutions contain an increased number of pollutants molecule, prohibiting light from reaching the surface of photocatalyst. As a result, lower numbers of hydroxyl radicals will be generated in the reaction mixture, which may be inadequate to eliminate the harmful contaminants [45]. However, as the reaction proceeds, the competitive absorption of dye molecules leads to a reduction in the number of oxygen and water moles adsorbed on the catalyst surface and as a result, less hydroxyl radicals are produced. Additionally, increasing the concentration of AB 74 causes UV light scattering. Furthermore, the electrons of the dye can be excited by the received energy from UV light. Thus, an increase in the concentration of dye leads to wasting the emitted light to the excited molecules of the dye, reducing the number of hydroxyl radicals produced by the photocatalyst [48,49].

The photocatalytic reaction of dye degradation can be obtained by a modified equation of Langmuir-Hinshelwood, shown by equation (5) [46].

$$-r = -\frac{dC}{dt} = \frac{k_c K_R C}{1 + K_R C_0} = k_{app} C \quad (11)$$

Whereas (k_c) is the kinetic rate constant of surface reaction, K_R is the Langmuir adsorption constant and C_0 is the initial dye concentration of solution. The photocatalytic degradation of dye follows a pseudo first order reaction, and k_{app} is the apparent rate constant of this reaction. The photocatalytic reaction rate constant for different dye concentrations can be determined by equation (6).

$$\ln\left(\frac{C}{C_0}\right) = -k_{app} t \quad (12)$$

In this equation, C_0 is initial dye concentration (mol. L⁻¹), and C depicts the dye concentration at any given time (mol. L⁻¹)

In Fig. 12, the photocatalytic reaction rate constant of WO₃: Co in various concentrations of the dye solution was obtained by plotting $\ln(C/C_0)$ versus irradiation time.

Table 4 shows that an increase in the dye concentration is followed by the reaction rate constant decreases. According to the results, when the dye concentration is increased from 20 ppm to 60 ppm, the photocatalytic reaction rate declines from 0.046 min⁻¹ to 0.0164 min⁻¹.

As mentioned, the Langmuir-Hinshelwood gives k_{app} as a function of k_c and K_R (equations (7) and (8)).

$$k_{app} = \frac{k_{obs} K_R}{1 + K_R C_0} \quad (13)$$

$$\frac{1}{k_{app}} = \frac{1}{K_R k_{obs}} + \frac{C_0}{K_R} \quad (14)$$

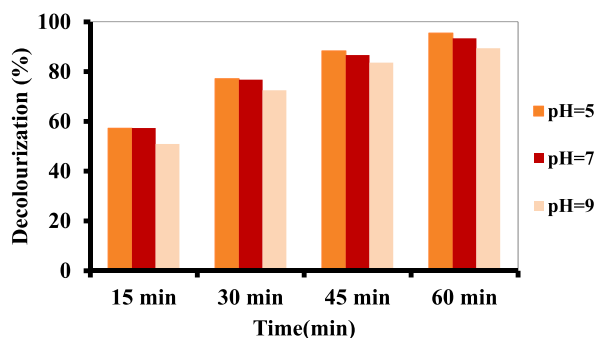


Fig. 10. Effect of pH of dye solution on photoactivity of WO₃: Co ([AB 74]₀ = 20 ppm, catalyst dosage: 0.2 g. L⁻¹).

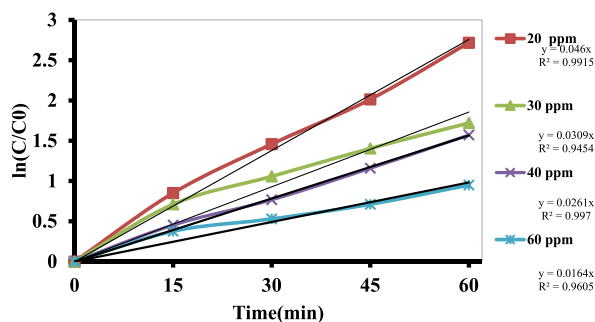


Fig. 11. Evaluation of reaction kinetics for different dye concentrations (catalyst dosage: 0.2 g L^{-1} , $t = 60 \text{ min}$, $T = 23 \text{ }^\circ\text{C}$).

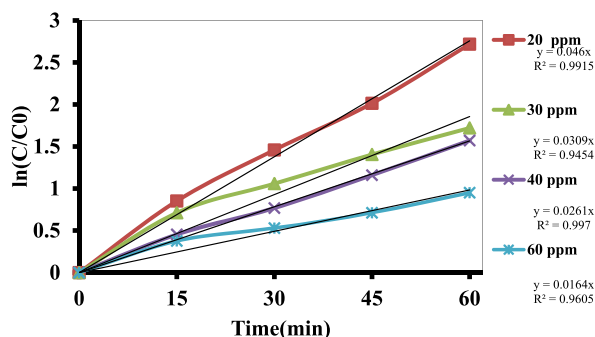


Fig. 12. Modified Langmuir plot of decolorization processes ($T = 23 \text{ }^\circ\text{C}$).

Table 4

Rate constant of photocatalytic reaction with different initial dye concentration.

Initial dye (ppm)	$k_{app} \text{ (min}^{-1}\text{)}$	R^2
20	0.046	0.9915
30	0.0309	0.9454
40	0.0261	0.997
60	0.0164	0.9605

The graph illustrating the changes of $1/k_{app}$ versus the initial dye concentration is used to determine the values of K_R and k_c , which were at 1.036 l mg^{-1} and $0.45 \text{ mg L}^{-1} \cdot \text{min}^{-1}$, respectively [50,51].

3.5. Effect of temperature

The reaction rate constant can be determined through the Arrhenius equation, which is related to the temperature. Equation (9)

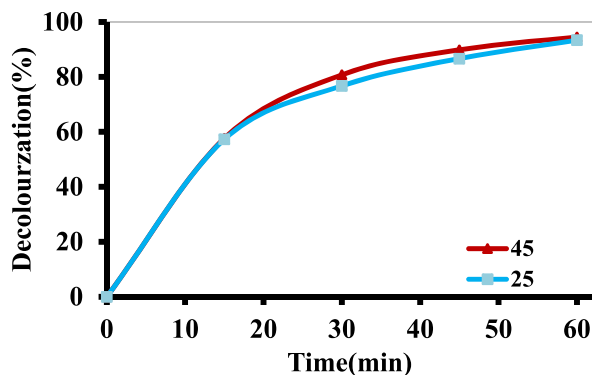


Fig. 13. Effect of temperature on rate of photoreaction ($[\text{AB 74}]_0 = 20 \text{ ppm}$, catalyst dosage: 0.2 g L^{-1} , $T = 23 \text{ }^\circ\text{C}$, and $45 \text{ }^\circ\text{C}$).

shows the Arrhenius equation:

$$k_{app} = A \exp \left[- \left(\frac{E}{RT} \right) \right] \quad (15)$$

In this equation, k_{app} is the photocatalytic reaction rate constant, A is the temperature-independent factor (for first-order reaction (s^{-1})), E is the activation energy ($J \cdot mol^{-1}$), R is the gas constant ($8.31 J K^{-1} mol^{-1}$), and T is the solution temperature.

Consequently, when the reaction temperature increases, k_{app} increases as well, and it is followed by enhancement of the semiconductor photocatalytic performance.

The effect of increasing catalyst's temperature was investigated by increasing the initial temperature of the solution to 45 °C. Fig. 13 indicates that by raising the temperature, which results in a slight increase in the reaction rate constant.

The typical temperature range for the textile industry's wastewater is in the range of 33–45 °C. Investigation of the temperature effect on the photocatalytic reaction was carried out at 45 °C to assess the possibility of maintaining the discharged wastewater temperature.

3.6. RSM modeling experiments

The experimental plan was designed based on the defined factors and the CCD model. As shown in Table 5, the designed experiments were performed with a reaction time of 45 min, and the corresponding experimental results were obtained.

The quadratic regression coefficients derived from the CCD experiments express the relationship of decolorization rate and the model parameters, referring to the model outlined by Antonopoulou et al., [48].

Table 5 illustrates the results of the experimental tests contrasted with the modeled data, presenting Y- experimental values in each row alongside their corresponding Y-predicted values derived from equation (10).

$$Y = 74.37 - 13.84x_1 + 9.54x_2 - 0.95x_3 + 2.59x_1^2 - 0.599x_2^2 + 0.70x_3^2 + 2.62x_1x_2 + 0.013x_1x_3 + 0.58x_2x_3 \quad (16)$$

The discrepancy between these values is quantified as error, displayed in the "Residuals" column. Evaluating the reproducibility of the experiment, essential for refining the accuracy of the RSM model, involves a meticulous examination of the consistency across specific rows, named as 1, 2, 4, 9, 12, and 19, pivotal central data points within the study.

The photocatalytic efficiency of the WO_3 : Co nanoparticles was estimated using equation (10), and the results are reported in Table 6.

Observation No. 17, with a residual of 5.483, is defined as the only unusual observation in this modeling, which is resulted by an error in the experiment.

The appropriateness of the proposed model can be assessed using the ANOVA table represented in Table 6. The coefficient of R^2 shows how well the estimated data aligns with the experimental data. R^2 values range from 0 to 1, and if this value is closer to 1, the model reveals a better accordance with the experimental data.

In this study, the value of R^2 was determined as 0.9686, which indicates a good fit of this regression model. However, it is worth noting that the high amount of R^2 doesn't necessarily guarantee that the model is appropriate. This value indicates an increase when additional variables are introduced to the model, regardless of being significant or non-significant. The value of the adjusted R^2 does

Table 5
Experimental and calculated decolorization of WO_3 : Co resulted by RSM model.

Run order	x_1	x_2	x_3	Y		Residuals
				Experimental	Predicted	
1	0	0	0	75.77	74.37375	1.39625
2	0	0	0	71.34	74.37375	-3.03375
3	-1	-1	-1	86.22	85.54855	0.671445
4	0	0	0	74.35	74.37375	-0.0237455
5	-1	1	-1	98.20	98.20635	-0.0023545
6	-1	0	0	86.65	90.81178	-4.16178
7	0	1	0	84.93	83.31978	1.61022
8	-1	1	1	99.07	97.46155	1.60845
9	0	0	0	74.56	74.37375	0.186255
10	0	-1	0	63.94	64.22898	-0.288982
11	1	-1	1	49.21	49.53795	-0.327955
12	0	0	0	73.94	74.37375	-0.433745
13	1	1	1	74.06	75.06175	-1.00175
14	1	1	-1	73.54	75.75455	-2.21455
15	-1	-1	1	84.34	82.45575	1.88425
16	0	0	1	71.97	74.13298	-2.16298
17	1	0	0	68.61	63.12698	5.48302
18	0	0	-1	79.51	76.02578	3.48422
19	0	0	0	73.64	74.37375	-0.733745
20	1	-1	-1	50.64	52.57875	-1.93875

Table 6
ANOVA table.

Source of variations	Sum of squares	Degree of freedom	Adjusted mean square	F-value	P-value
Regression	2931.39	9	325.71	34.23	0.000
Residual	95.16	10	9.52		
Total	3026.54	19			

$$R^2 = 96.86 \% \quad R_{\text{adj}}^2 = 94.03 \% \quad R_{\text{pred}}^2 = 78.33 \%$$

not always increase when the added variables show an incorporation into the model. In fact, if non-significant terms are added to the model, the value of R_{adj}^2 may decrease as well. Therefore, a substantial difference between R^2 and R_{adj}^2 reveals the presence of unnecessary and nonsignificant terms in the model [36,48].

In this study, the R_{adj}^2 is calculated at 0.9403. The high R_{adj}^2 value indicates that the model is highly significant. In addition, the close values of R^2 and R_{adj}^2 reflect a small number of non-significant terms in the model.

The regression p-value less than 0.05 indicates the quadratic model used in the modeling is significant. The P-value for the parameters of the dye concentration and catalyst dosage are both zero, and the interaction between these two parameters is 0.037, indicating that these three parameters play a significant role in the proposed model.

Obtained R-square shows that 97 % of the theoretical data obtained in the regression model corresponds with the experimental values. Fig. 14 illustrates that most of the variance calculated by the regression model is in close agreement with the obtained experimental data, with these experimental points aligning closely with the regression line.

Fig. 15a, the normal distribution of residuals is investigated. In this case, most of the residual points have accumulated around the blue line, representing the error terms are normally distributed. A high value of R^2 can be indicative of an appropriate model when residuals are in insignificant amounts. As can be observed in Fig. 15b, residuals ranging from -5 to 5 % and are evenly distributed above and below the zero line.

Fig. 15c illustrates that the substantial amounts of residuals are in the range of -2 to 2 , reaffirming the normal distribution of residuals. Fig. 15d shows a normal distribution of residuals.

The obtained results show that the regression model fitted well with the experimental data.

Fig. 16 shows how the decolorization efficiency changes as a function of three pairs of factors: catalyst dosage and pH, dye concentration and catalyst dosage, and dye concentration and pH of dye solution, respectively.

The optimal conditions, as explained in the model, include an initial dye concentration of 20 ppm [AB 74]₀, which has been previously studied for various transition metals doped into the crystallite structure of WO_3 [28]. Additionally, the optimal catalyst dosage is at 0.24 g. L^{-1} and a pH of 5.

Fig. 17 illustrates the photocatalytic efficiency of WO_3 : Co under these conditions. The experimental result demonstrates a 98.204 % decolorization, closely matching the model's prediction of a 98.2064 % decolorization rate within the reaction time of 45 min.

In addition, Fig. 17 represents the total TOC analysis of dye solution in this reaction indicating a 30 % degradation of organic compound within 60 min.

As a result of photocatalyst dosage evaluation, it is evident that increasing the catalyst dosage for an excess amounts of 0.2 g. L^{-1} , is led by diminishing the slope of photocatalytic enhancement rate efficiency. Therefore, the amounts exceeding the optimum dosage, which was found in RSM modeling, is not economically justified.

4. Reusability

To further understand the photodegradation and economic efficiency of the new prototype of the Co: WO_3 nano photocatalysts, we investigated the reusability of the nanoparticles. The recycling studies of Co: WO_3 were performed using the obtained optimum amount of the nanoparticle at 0.2 mg , a dye concentration of 20 ppm, a pH of 7, and a reaction time of 60 min. The nanoparticles were filtered and collected after each cycle, and then placed in the oven for 12 h at $100 \text{ }^\circ\text{C}$. The reaction was examined for 0.2 mg of the photocatalyst powder. The exact reaction procedure was repeated for each run, and the results are illustrated in Fig. 18. As depicted, the photocatalytic efficiency dropped by 15.64 % (from 92 to 76.36 %) and 33.12 % (from 92 to 58.88 %) after the first and second cycles, respectively. However, it decreased significantly after the third cycle, reaching 53.36 % (from 92 to 38.64 %). The observed results confirmed that the Co: WO_3 photocatalyst has acceptable recyclability, although after the third cycle, the photodegradation rate decreased to around 38.64 %. Several factors can reduce the photodegradation efficiency, including a reduction in the active surface area being occupied by the contaminants' molecules. This can be overcome by treating the photocatalyst with acid-base treatment to maintain the generation of hydroxyl groups [49,52].

5. Conclusion

In recent years, WO_3 based photocatalysts have attracted significant interest in the field of visible light photocatalytic reactions, because of their narrow bandgap, low cost, stability, and non-hazardous properties. Co doped WO_3 nanoparticles, synthesized by the microwave-assisted solution combustion method, and amorphous structure of WO_3 were formed due to fast and brief time of combustion reaction.

After annealing at $400 \text{ }^\circ\text{C}$ for an hour, a phase transformation from monoclinic to orthorhombic occurs. XRD patterns revealed the

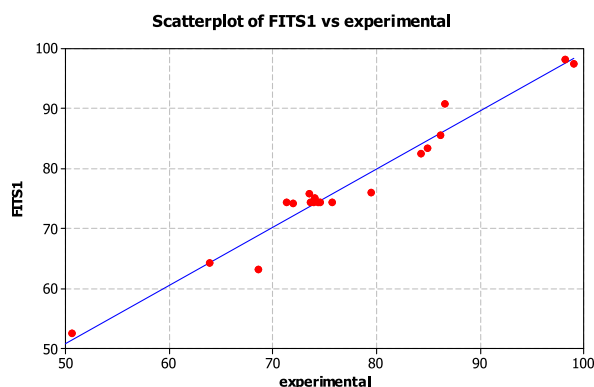


Fig. 14. Scatter plot of fits again experimental data.

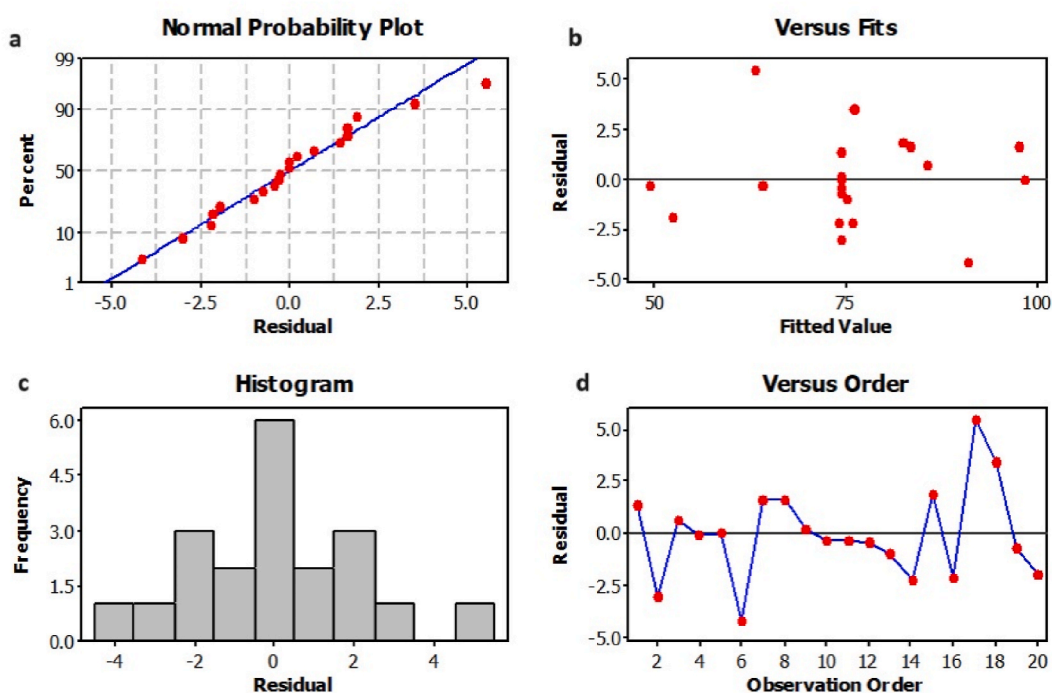


Fig. 15. Residual plots of RSM model.

broad short peaks, which revealed the amorphous structure of the compound.

The SEM images revealed the agglomerated nanoparticles, forming amorphous masses, and the dimensions of the produced nanoparticles were smaller than 200 nm. The EDS analysis detected 0.5 wt% of Co on the surface of the photocatalyst.

The photocatalytic performance was evaluated by the photodegradation of AB 74 dye, and examined the effect of the initial dye concentration, pH, and the temperature of the dye solution on the photocatalytic reaction. The optimum conditions were determined as a catalyst dosage of 0.2 g. L⁻¹ and a pH = 5. Increasing the dye concentration reduced the reaction rate, and the investigation of the effect of temperature demonstrated that the photocatalytic reaction was an endothermic nature of the photocatalytic reaction, with higher rates at elevated temperatures.

The photocatalyst experiments were designed using RSM modeling in Minitab 16 software. The experimental and calculated decolorization efficiencies were in excellent agreement. The WO₃: Co photocatalyst indicated a complete degradation of AB 74 under the optimum conditions determined by the regression model, with a reaction time of 45 min.

It has been concluded that WO₃-based photocatalysts, is not only environmentally friendly photocatalyst to be used in removing organic pollutants from wastewater, but also when combined with elemental semiconductors to form a composite, can be used as a visible light photocatalyst, and it doesn't possess the limitations of other semiconductors such as TiO₂ and ZnO. It has special chemical and physical properties such as large surface area, small bandgap energy, and energy storage potential [42]. Co: WO₃ showed

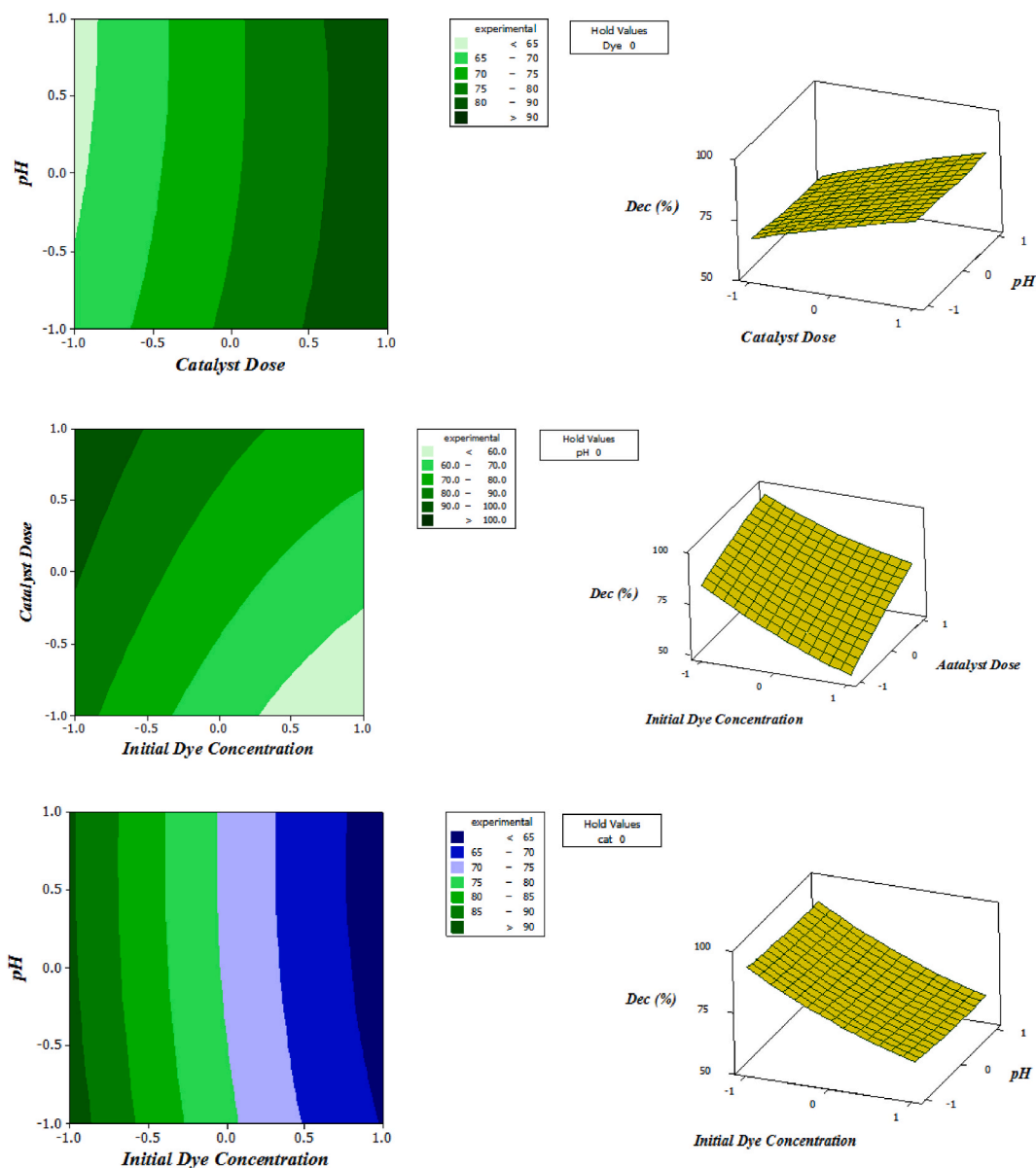


Fig. 16. Effect of parameters and their interactions on decolorization efficiency.

acceptable performance and reusability in three consecutive cycles. The removal efficiency in four cycles were at 92 %, 76.36 %, 58.88 %, and 38.64 %, respectively. The photodegradation process occurs through holes (h^+) and hydroxyl radicals ($\bullet OH$). The reduction in the photodegradation efficiency can be attributed to the occupation of active sites on the surface of the photocatalysts by the dye molecules, resulting in reduced light contact and a decrease in hydroxyl radical generation.

Funding statement

This study did not receive any specific grant from funding agencies in the public, commercial, or not-for-profit sectors.

Data availability statement

The data that support the findings of this study are available on request from the corresponding author.

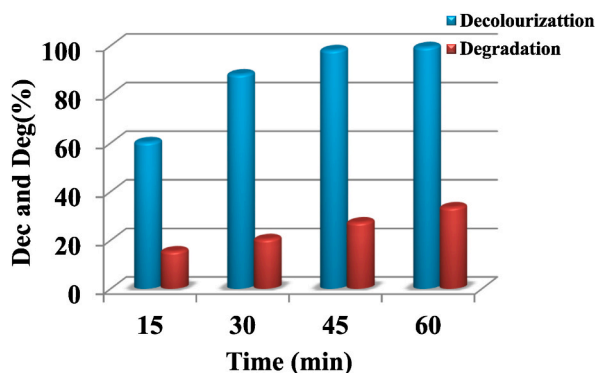


Fig. 17. Decolorization and degradation of AB 74 by WO₃:Co in the optimum point of three factors (catalyst dosage = 0.2 g. L⁻¹, [AB 74]₀ = 20 ppm, pH = 5).

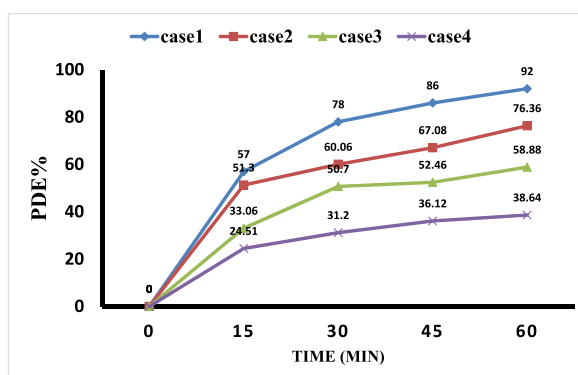


Fig. 18. Reusability of the Co: WO₃ photocatalyst for AB 74 degradation (dye concentration - 20 ppm, catalyst mass - 0.2 mg, pH - 7, time - 60 min).

CRedit authorship contribution statement

Leila Montazerghaem: Supervision, Investigation, Formal analysis. **Mitra Keramatifarhodbonab:** Writing – review & editing, Investigation, Data curation. **Alireza Naeimi:** Supervision, Project administration, Investigation, Data curation.

Declaration of competing interest

The authors declare that they have no known competing financial interests or personal relationships that could have appeared to influence the work reported in this paper.

References

- [1] S. Pang, et al., Natural wood-derived charcoal embedded with bimetallic iron/cobalt sites to promote ciprofloxacin degradation, *J. Clean. Prod.* 414 (2023) 137569.
- [2] Y. Dong, et al., A novel conditioning approach for amelioration of sludge dewaterability using activated carbon strengthening electrochemical oxidation and realized mechanism, *Water Res.* 220 (2022) 118704.
- [3] Z. Wang, et al., Bamboo charcoal fused with polyurethane foam for efficiently removing organic solvents from wastewater: experimental and simulation, *Biochar* 4 (2022) 28.
- [4] Y. Yan, et al., Merits and limitations of radical vs. nonradical pathways in persulfate-based advanced oxidation processes, *Environ. Sci. Technol.* 57 (2023) 12153–12179.
- [5] W. Sun, et al., Characteristics and application of iron-based materials in heterogeneous Fenton oxidation for wastewater treatment, A review. *Environmental Science: Water Research and Technology* 9 (2023) 1266.
- [6] P. Xia, et al., MOF-derived single-atom catalysts: the next frontier in advanced oxidation for water treatment, *Chemical Engineering* 452 (2023) 139446.
- [7] E.M. Saggioro, et al., Effect of activated carbon and titanium dioxide on the remediation of an Indigoid dye in model waters, *Rev. Chim-Bucharest.* 65 (2014) 237–241.
- [8] P. Olusakin, et al., Methylene blue dye: toxicity and potential elimination technology from wastewater, *Results in Engineering* 16 (2022) 100678.
- [9] E.M. Saggioro, et al., Photo-decolorization and ecotoxicological effects of solar compound parabolic collector pilot plant and artificial light photocatalysis of indigo carmine dye, *Dyes Pigments* 113 (2015) 571–580.
- [10] Z. Zainal, et al., Removal of dyes using immobilized titanium dioxide illuminated by fluorescent lamps, *J. Hazard Mater.* 125 (2005) 113–120.

- [11] E.S. Agorku, et al., Palladium-decorated zinc sulfide/reduced graphene oxide nanocomposites for enhanced visible light-driven photodegradation of indigo carmine, *Mat. Sci. Semicon. Proc.* 33 (2015) 119–126.
- [12] N. Barka, et al., Photocatalytic degradation of indigo carmine in aqueous solution by TiO₂-coated non-woven fibers, *J. Hazard Mater.* 152 (2008) 1054–1059.
- [13] N. Koprivance, et al., AOP as an effective tool for the mineralization of hazardous organic pollutants in colored wastewater; chemical and photochemical processes, in: A.A. Lewinsky (Ed.), *Hazardous Materials and Wastewater: Treatment, Removal and Analysis*, Nova Science Publishers Inc., New York, 2007, pp. 149–199.
- [14] C. Zaharia, et al., Characteristics, polluting effects and separation/elimination procedures from industrial effluents- A critical overview in: Puzyn, T., Mostrag-Szlichtyng, A. *Organic pollutants ten Years after the Stockholm convention environmental and analytical Update*, In tech. (2012) 55–89.
- [15] A.L.N. Mota, et al., Advanced oxidation processes and their application in the petroleum industry_ a review, *Brazilian Journal of Petroleum and Gas* 2 (2008) 122–142.
- [16] Hernández-Ramírez, et al., *Photocatalytic Semiconductors, Synthesis, Characterization, and Environmental Applications*, Springer International Publishing., Switzerland, 2015, pp. 1–40.
- [17] Y. Zheng, et al., Sulfur-doped g-C₃N₄/rGO porous nanosheets for highly efficient photocatalytic degradation of refractory contaminants, *Journal of materials science and technology* 41 (2020) 117–126.
- [18] M. Mansoob Khan, Metal oxides as photocatalysts, *J. Saudi Chem. Soc.* 19 (2015) 462–464.
- [19] Fatima Aziz, et al., Zinc oxide-tungsten oxide (ZnO-WO₃) composite for solar light-assisted degradation of organic dyes, *Kor. J. Chem. Eng.* 40 (2023) 1497–1509.
- [20] U. Alam, et al., Direct Z-scheme-based novel cobalt nickel tungstate/graphitic carbon nitride composite: enhanced photocatalytic degradation of organic pollutants and oxidation of benzyl alcohol, *Colloids Surf. A Physicochem. Eng. Asp.* 630 (2021) 127606.
- [21] V.M. Ndumiso, et al., Adsorption and photocatalytic degradation of dye contaminants in wastewater over W-doped titania nanotubes, *J. Taiwan Inst. Chem. Eng.* 146 (2023) 104863.
- [22] Sánchez-Martínez, et al., Synthesis of WO₃ nanoparticles by citric acid-assisted precipitation and evaluation of their photocatalytic properties, *Mater. Res. Bull.* 48 (2013) 691–697.
- [23] L. Zhixiang, et al., Synthesis of high surface area monoclinic WO₃ particles using organic ligands and emulsion-based methods, *Journal Materials Chemistry* 12 (2002) 983–989.
- [24] H. Pengfei, et al., One-step thermal compensation decomposition synthesis of ZnWO₄/WO₃ composite with synergy of multiple structural effects for efficient trace H₂S detection, *Sensors and Actuators: B. Chemical.* 381 (2023) 133388.
- [25] Z. Yan, et al., WO₃ nanoparticle synthesized through ion exchange route as Pt electrocatalyst support for alcohol oxidation, *Fuel Cell* 14 (2014) 291–295.
- [26] Martínez-de la Cruz, et al., Synthesis and characterization of WO₃ nanoparticles prepared by the precipitation method: evaluation of photocatalytic activity under vis-irradiation, *Solid State Sci.* 12 (2010) 88–94.
- [27] A. Naeimi, et al., Transition metals doped WO₃ photocatalyst towards high efficiency decolorization of azo dye, *J. Mol. Struct.* 1250 (2022) 131800.
- [28] A. Kopp Alves, et al., Combustion synthesis, in: *Novel Synthesis and Characterization of Nanostructured Materials*, Springer Berlin Heidelberg, Berlin, 2013, pp. 11–22.
- [29] B. Manoj, et al., Microwave-assisted chemistry: synthetic applications for rapid assembly of nanomaterials and organics, *Accounts of Chemical Research* 47 (2014) 1338–1348.
- [30] E. Gutiérrez-Segura, et al., Sorption of indigo carmine by a Fe-zeolitic tuff and carbonaceous material from pyrolyzed sewage sludge, *J. Hazard Mater.* 170 (2009) 1227–1235.
- [31] M.S. Secula, et al., An experimental study of indigo carmine removal from aqueous solution by electrocoagulation, *Desalination* 277 (2011) 227–235.
- [32] M. Pomeroy, *Encyclopedia of Materials: Technical Ceramics and Glasses*, book, 2021.
- [33] Weizhen Liu, et al., Effective extraction of Cr (VI) from hazardous Gypsum sludge via controlling the phase transformation and chromium species, *Environ. Sci. Technol.* 52 (2018) 13336–13342.
- [34] Zeyu Wang a, Enhanced adsorption and reduction performance of nitrate by Fe–Pd–Fe₃O₄ embedded multi-walled carbon nanotubes 281 (2021) 130718.
- [35] R.H. Myers, *Building Empirical Models, Response Surface Methodology: Process and Product Optimization Using Designed Experiments*, forth ed., Jhon Wiley & sons, New Jersey, 2009.
- [36] -H. Cho II, K.-D. Zoh, Photocatalytic degradation of azo dye (Reactive Red 120) in TiO₂/UV system: optimization and modeling using a response surface methodology (RSM) based on the central composite design, *Dyes Pigments* 75 (2007) 533–543.
- [37] M.A. Bezerra, et al., Response surface methodology (RSM) as a tool for optimization in analytical chemistry, *Talanta* 76 (2008) 965–977.
- [38] G Rajput Kaur, et al., Influence of Ag substitution on structural and optical properties of tungsten oxide, *Indian J. Phys.* 97 (2023) 2053–2060.
- [39] K. Xueying, et al., Synthesis of Co-doped SnO₂ nanofibers and their enhanced gas-sensing properties, *Sensor. Actuator. B Chem.* 236 (2016) 425–432.
- [40] M.H. Ahmadi Azghandi, Synthesis of Cd doped ZnO/CNT nanocomposite by using microwave method: photocatalytic behavior, adsorption and kinetic study, *Results Phys.* (2017) 1106–1114.
- [41] Abdullah Al Mamuna, et al., Structural, electronic, optical properties and molecular dynamics study of WO₃ W0.97Ag0.03O₃ and W0.94Ag0.06O₃ photocatalyst by the first principle of DFT study, *Egyptian Journal of Chemistry* 64 (2021) 5117–5126.
- [42] Idrees Khana, et al., Heterogeneous photodegradation of the industrial dyes: an insight to different mechanisms and rate affecting parameters, *J. Environ. Chem. Eng.* 8 (2020) 104364.
- [43] S.A. Abo-Farha, et al., Photocatalytic degradation of monoazo and diazo dyes in wastewater on nanometer-sized TiO₂, *Researcher* 2 (2010) 1–20.
- [44] R. Marandi, et al., Kinetic modeling of photocatalytic degradation of an azo dye using nano-TiO₂/polyester, *Environ. Eng. Sci.* 29 (2012) 957–963.
- [45] M. Rani, et al., Sunlight assisted highly efficient photocatalytic remediation of organic pollutants by green biosynthesized ZnO@WO₃ nanocomposite, *Journal of Photochemistry and Photobiology, A: Chemistry.* 446 (2024) 115160.
- [46] H. Sudrajat, et al., Comparison and mechanism of photocatalytic activities of N-ZnO and N-ZrO₂ for the degradation of rhodamine 6G, *Environ. Sci. Pollut. Res.* 23 (2016) 10177–10188.
- [47] M.F. Hanafi, Effect of pH on the photocatalytic degradation of Remazol brilliant blue dye using zirconia catalyst, *Mater. Today: Proc.* 31 (2020) 260–262.
- [48] M. Antonopoulou, et al., Photocatalytic reduction of Cr (VI) by char/TiO₂ composite photocatalyst: optimization and modeling using the response surface methodology (RSM), *Environ. Sci. Pollut. Res.* (2016) 1–11.
- [49] M. Samy, et al., Photocatalytic degradation of trimethoprim using S-TiO₂ and Ru/WO₃/ZrO₂ immobilized on reusable fixed plates, *Journal of Water Process Engineering* 33 (2020) 101023.
- [50] K. Yetilmezsoy, et al., Response surface modeling of Pb(II) removal from aqueous solution by Pistacia vera L.: Box-Behnken experimental design, *J. Hazard Mater.* 171 (2009) 551–562.
- [51] O. Samuel, et al., WO₃-based photocatalysts: a review on synthesis, performance enhancement and photocatalytic memory for environmental applications, *Ceram. Int.* 48 (2022) 5845–5875.
- [52] M.A. Barakat, et al., Sustainable visible light photocatalytic scavenging of the noxious organic pollutant using recyclable and reusable polyaniline coupled WO₃/WS₂, *J. Clean. Prod.* 330 (2022) 129942, nanohybrid.